



Automatic quantification of spheroidal graphite nodules using computer vision techniques

Renato F. Pereira¹ · Valberto E. R. da Silva Filho¹ · Lorena B. Moura¹ · N. Arun Kumar² · Auzuir R. de Alexandria¹ · Victor Hugo C. de Albuquerque³

© Springer Science+Business Media, LLC, part of Springer Nature 2018

Abstract

The microstructure of nodular cast irons is characterized by the presence of spheroidal graphite nodules. Metallographic tests may show irregular or degenerated graphite nodules that indicate a reduction in tensile strength of the material as well as its yield limit. This work proposes a computer vision algorithm to estimate the amount of degenerated graphite nodules as well as image analysis necessary to determine the relationship between this quantity of degenerated nodules and the loss of mechanical properties of the nodular cast iron. The proposed algorithm was tested using two cast iron samples, by measuring their microhardness and tensile strength. The results show that the amount of degenerated graphite nodules is inversely proportional to the limit of traction resistance. Sample “A”, of the two samples tested, presented more degenerated nodules than “B” and a lower limit of traction resistance; therefore, it needs less strength to break.

✉ Auzuir R. de Alexandria
auzuir@ifce.edu.br

Renato F. Pereira
renato.francisco.pereira@gmail.com

Valberto E. R. da Silva Filho
valbertoenoc@gmail.com

Lorena B. Moura
lorenabraga@ifce.edu.br

N. Arun Kumar
arun.nura@gmail.com

Victor Hugo C. de Albuquerque
victor.albuquerque@unifor.br

¹ Instituto Federal de Educação, Ciência e Tecnologia do Ceará - IFCE, Fortaleza, Ceará 60040-531, Brazil

² Department of Electronics and Instrumentation, SASTRA University, Thanjavur 613401, India

³ Programa de Pós-Graduação em Informática Aplicada, Laboratório de Bioinformática, Universidade de Fortaleza, Fortaleza, Ceará 60811-905, Brazil

Keywords Cast iron · Microstructural characterization · Quantitative metallography · Computer vision techniques

1 Introduction

Nodular cast irons are being used more frequently in highly stressed components, particularly in the automotive industry [4,33]. Therefore, it is essential to thoroughly understand the factors influencing the fatigue properties of these materials [22,46]. In spheroidal graphite cast irons, two types of defects may act as preferential sites for fatigue crack initiation and growth [39]. Graphite nodules with diameter around 420 μm are one of these sites [7].

Quantitative microstructure analyses are central to materials engineering and design [11,13,16,36]. Traditionally, this entails careful measurements of volume fractions, size distributions, and shape descriptors of familiar microstructural features such as grains and second-phase particles [8,17,27]. These quantities are connected to theoretical and/or empirical models for material properties, e.g., grain boundary or particle-strengthening mechanisms [25,26,28].

Their fatigue strength depends on the structure of the matrix and the characteristics of the spheroidal graphite and casting defects [2]. In many cases, fatigue fracture is caused by casting defects; however, their fatigue strength can be improved by decreasing the number of casting defects that exist near the surface [12,18,29,37].

There is a lot of work in the literature on gray and austempered ductile irons but little work on nodular cast iron with a ferritic matrix [3,23,24,45].

The initial microstructure of nodular cast irons consists of graphite nodules surrounded by ferrite and some perlite. The average microhardness of the unprocessed material is approximately 150 HV [5]. A fully ferrite matrix is as cast without any heat treatment [10]. The volume fraction of nodules is 10% with a mean size of 15 μm and a ferrite grain size of 50 μm [6,35].

The main contribution of this work is the correlation observed between the degenerated graphite and the mechanical properties of nodular cast iron. Also, an important contribution was the development of a computer vision algorithm capable of quantifying the degenerated nodules present in sample images of the spheroidal graphite cast iron. This algorithm helped understand the correlation between the degree of spheroidization and the respective mechanical responses of the analyzed material. The presented methods use mainly classification approaches to quantify microstructure characterization; therefore, they need a training phase, which tends to be a long process and in need of large amounts of data to achieve acceptable results [44]. This paper, however, proposes a simpler approach to this problem, relying mainly on image processing techniques to mimic human inspection. Not only that, but studies to determine the relationship between the degenerate nodules to the degradation of the mechanical properties of the material, namely, tensile strength in nodular cast iron, were not found in the literature.

This paper is organized as follows: Sect. 2 presents related works and explains the approach of each work. Section 3.1 presents the mechanical tests performed in this work. Section 3.2 presents the techniques used in the CV algorithm, showing the

steps and explaining the method. Section 4 presents the results after applying the CV algorithm to the images and the correlation with the data generated by the mechanical tests. Finally, Sect. 5 presents the conclusion of this work and the results.

2 Related works

Papa et al. [40] reported that the automatic characterization of particles in metallographic images has been paramount, mainly because of the importance of quantifying such microstructures in order to assess the mechanical properties of materials commonly used in industry [14,20]. These authors use machine learning classification techniques to do this, specially support vector machine, Bayesian, and optimum-path forest-based classifiers, as well as Otsu's method, which is commonly used in computer imaging to automatically binarize images. Otsu's method was also used in this work, where it demonstrated the need for more complex methods in the evaluation of characterization of graphite particles in metallographic images [41]. The optimum-path forest-based classifier demonstrated an overall superior performance, both in terms of accuracy and speed.

de Albuquerque et al. [11] presented a similar work, in which they compare two classifiers with different approaches for the task of microstructure segmentation. The first was an MLP (multilayer perceptron), a class of neural network supervised with backpropagation as the training method, and the second classifier was self-organizing map (SOM), which is an unsupervised machine learning algorithm that was proposed by Kohonen. The results showed the MLP performed similarly to human inspection.

de Albuquerque et al. [15] also presented a different system called SVRNA (segmentation by artificial neural network) for a study in the field of quantitative metallography applied to materials science. This system is used to characterize volumetric fractions of phases and grain size, as well as to determine inclusion distributions, among other parameters that influence the properties of materials, like nodular cast irons. This system is composed of a neural network with 42 neurons distributed in three layers. The neuron distribution corresponds to: 3 inputs, 30 neurons in the intermediate layer, and 9 neurons in the output layer. The inputs of the neural network are the R, G, and B components of each pixel. The output of the network, in turn, is the indication of which region, i.e., which color, should be assigned to the pixel under analysis.

The method mainly uses classification approaches to quantify the microstructure characterization; therefore, a training phase is needed, which tends to be a long process and requires large amounts of data to achieve acceptable results. In this work, we propose a simpler approach to this problem, and it relies mainly on image processing techniques to mimic human inspection. Studies to determine the relationship between the degenerated nodules and the reduction in the mechanical properties of the material, namely tensile strength in nodular cast iron, were not found in the literature.

3 Materials and methods

Figure 1 illustrates the purpose of this article. In summary, two samples are subjected to metallographic, microhardness, and traction test. Subsequently, the metallographic images are processed with CV techniques. The resulting image is then analyzed and relationships between the characteristics of the image and the mechanical properties of the material can be established.

3.1 Mechanical tests

The identification and validation of mechanical models used to predict the behavior of materials and structures are still the central focus of experimental mechanics. The ever-increasing sophistication of these mechanical models and the multiplicity of the scales required to assess and quantify the microscopic phenomena at play also present challenging demands to mechanical tests [19,31].

In this work, two samples of nodular cast iron from different manufacturers were used. The samples were cylindrical with diameters of 44 mm and 28 mm as shown in Fig. 2.

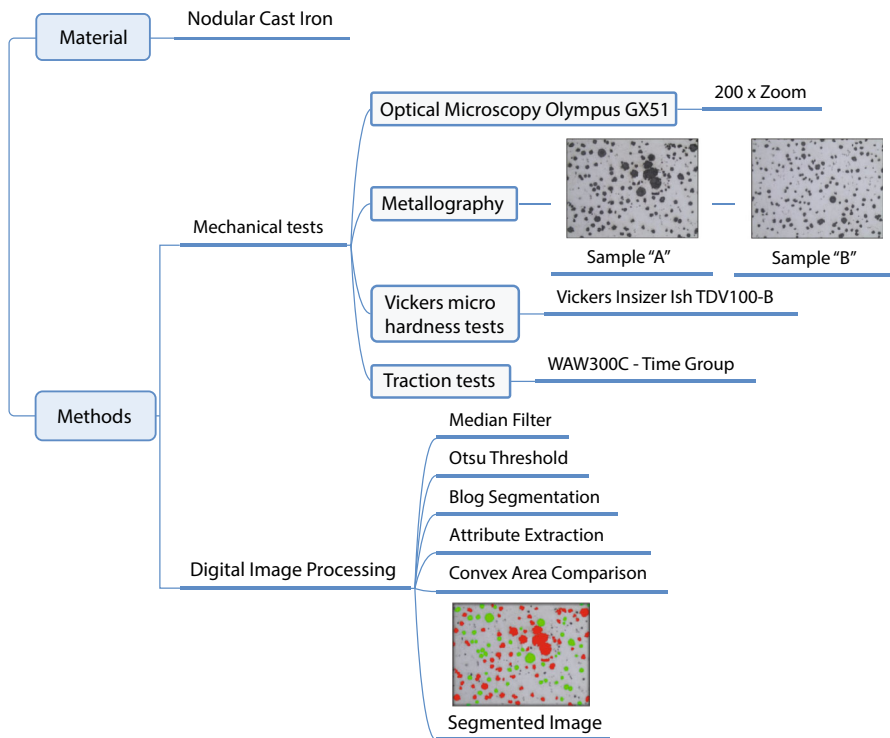


Fig. 1 Graphical abstract of the methodology

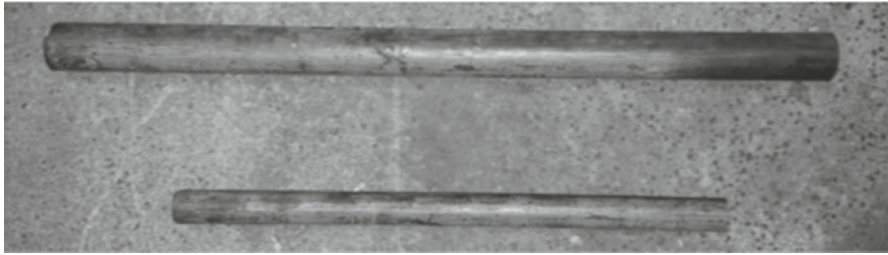


Fig. 2 Samples of nodular cast iron. Sample “A” above and “B” below

The approximate chemical composition of nodular cast iron is: carbon (2 to 4%), manganese (0.3 to 1%), silicon (1 to 3%), phosphorus (0.1 to 1%), sulfur (0.05 to 0.25%), and iron [6,21].

3.1.1 Metallography

The samples for the metallography assays were cut in the alternative saw into 15 mm length.

After cutting metallographic preparation was performed, sanding steps (up to 1200 mesh porosity), alumina and then etched with Nital 2% solution for 5 s to reveal the microstructure. Optical microscopy was performed on an Olympus GX51 microscope with Analysis Olympus software. The micrographs (Fig. 3) that could be seen under the microscope were captured by a computer connected to the microscope. All images were captured with a $200\times$ zoom. These images were used to develop the CV software, which is explained in more detail in a later topic.

This process was carried out several times for both samples. The 44-mm-diameter sample was called “A” (Figure 3.1.1), and the 28-mm-diameter sample “B” (Figure 3.1.1). About 40 images for each sample were captured, to represent the surface for analysis as accurately as possible.

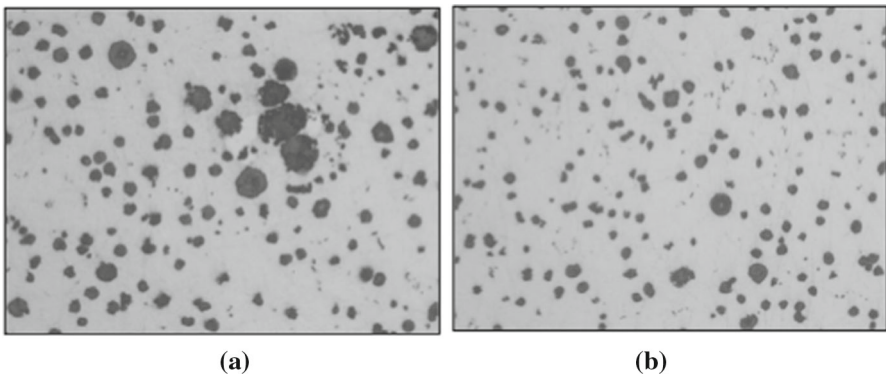


Fig. 3 Micrographs a sample “A”, b sample “B”

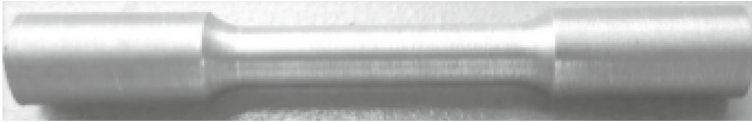


Fig. 4 Test body used in the traction test. Sample “B”

3.1.2 Traction tests

The traction test was carried out after the test bodies (Fig. 4) “A” and “B” had been prepared.

The equipment used for the test (WAW300C—Time Group), consists of two heads, one upper (fixed) and one lower (mobile). In each head, there is a claw that holds the test body. At the start of the test, the lower head descends slowly, executing the pulling force. The equipment is connected to a computer that has process monitoring software, where it is possible to select the elongation value and then the machine applies the force corresponding to this elongation. The elongation selected in the test was $0.5 + 15\%$ mm/min.

Knowing that cast irons are generally fragile, the test body practically did not undergo any narrowing.

During the test, the software shows a tension \times time graph in real time, which characterizes the time required to reach the limit of traction resistance (LRT) that is shown at the end of the test. Figure 5 shows the samples fractured after the test.

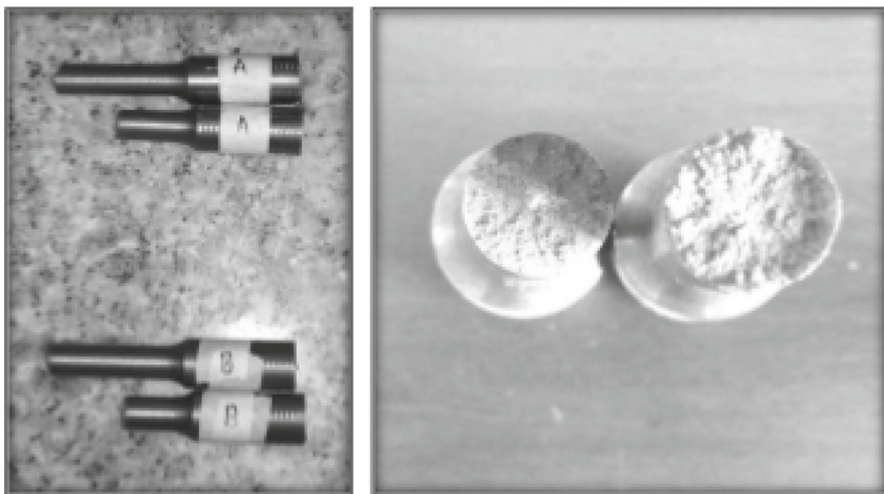


Fig. 5 Samples fractured after traction tests

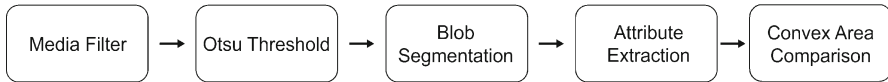


Fig. 6 Algorithm flowchart

3.1.3 Vickers microhardness tests

The microhardness values were acquired using Vickers hardness test very similar to a conventional hardness test, but with a much smaller diamond: only 7 mm long. The equipment used was a Vickers Insizer Ish—TDV1000-B. The diamond makes a microscopic perforation by applying a ranging from 0.1 to 1 kg f. The test body used is the same as the one used for the metallography test, since it already has a polished surface [42]. After drilling, the selected diamond diagonals are used to compute the resulting hardness. The load used was 0.5 kg f per 10 s. No norm was found regarding time and the load applied; therefore, these values were chosen because they are used generically for a large majority of materials; however, the choice of the values here was for comparison purposes only.

3.2 Computer vision algorithm

According to Fig. 6, the first step in developing the algorithm is to apply a median filter to remove any noise from the image. The best-known order statistics filter is the median filter, which replaces the value of a pixel by the median of the gray levels in the neighborhood of that pixel. The original value of the pixel is included in the computation of the median. Median filters are commonly used because they have excellent noise reduction capabilities for certain types of random noise, with considerably less blurring than linear smoothing filters of a similar size [30].

Subsequently, an Otsu threshold is applied, a nonparametric and unsupervised method of automatic threshold selection for picture segmentation. An optimal threshold is selected by the discriminant criterion, in order to maximize the separability of the resultant classes in gray levels. The procedure is very simple, using only the zeroth- and the first-order cumulative moments of the gray-level histogram [38]. Following this procedure, the nodules are in black and the ferritic matrix is in white, and therefore it is easier to distinguish the nodules from all other microstructures.

Then, a segmentation algorithm is applied. Region growing is a segmentation technique considered to be robust, fast, and free of tuning parameters. The method, however, requires the input of a number of seeds, either individual pixels or regions, which will control the formation of regions into which the image will be segmented [1]. This technique is able to group pixels from a pixel seed, with a previously specified stopping criterion. This technique was implemented by the Blob library wrapper around OpenCV (open-source computer vision) and a popular CV library [48], which is also able to store in simple data structures information about the nodules, in order to facilitate the extraction and calculation of points of interest of each node, e.g., coordinates of the edge and coordinates of the center of the nodules.

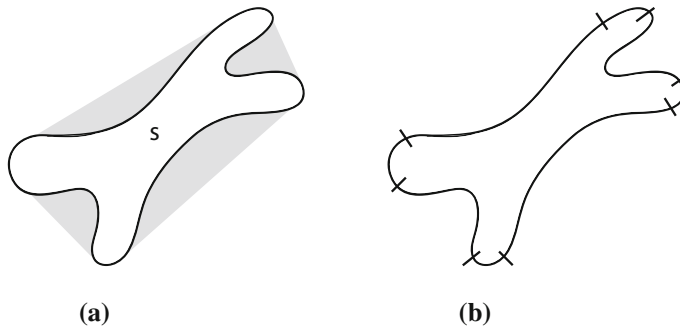


Fig. 7 Convex area representation, **a** convex area, **b** concave area

In order to differentiate the degenerated nodules from the normal ones, the concave and convex areas of the nodules were computed. The concave area (Fig. 7b) is the area of the nodule itself, and the area the convex nodule is the area that its surface occupies, as shown in Fig. 7a.

Using these two areas, the concave area was divided by the convex, generating a value that ranges from 0 to 1. The concave area can never be larger than the convex area, so that this value is close to 1 when the nodule is normal because it approaches a sphere and when the nodule is degenerated, the value is less than 1. A threshold value of 0.4 was empirically chosen to better represent degenerated nodules, in such a way that the nodules with this a ratio value less than 0.4 would be considered degenerated.

4 Results

The sample test bars were initially cast, and at the end of the bar a completely homogeneous structure was expected. To demonstrate this, three traction tests were performed on the test bodies extracted from each bar; thus, similar results would indicate that the bar is in fact homogeneous. The following graphs (Fig. 8) present the results of the traction tests.

The results show that the three test bodies of sample “A” fractured with a force of 58 kN and the three test bodies of sample “B” fractured at 62 kN.

The *ReL* point represents the stress at the flow limit, and the *FeL* point represents the strength at the flow limit. These points show the transition moment from the elastic deformation to the plastic deformation. On the other hand, the *Rm* point represents the tensile strength limit voltage and the *Fm* point represents the maximum strength. These points show the moment where the fracture occurs in the test body.

Table 1 shows the approximate values of *Fm* for all three tests and their algebraic average.

Table 2 shows the results of the Vickers microhardness tests of the samples “A” and “B”.

The CV algorithm verifies which nodules have the concave/convex area ratio of each nodule less than 0.4; these are then considered to be considered a degenerated

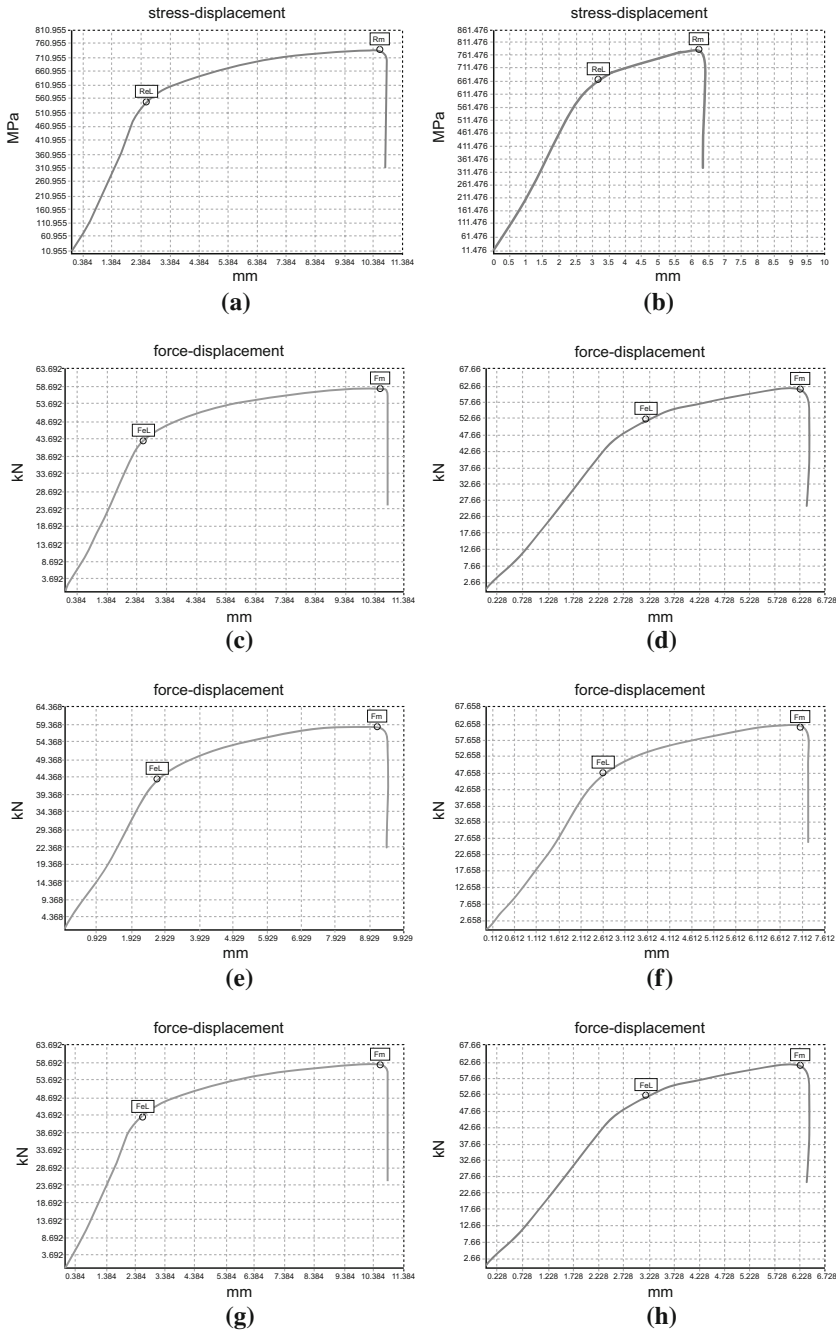


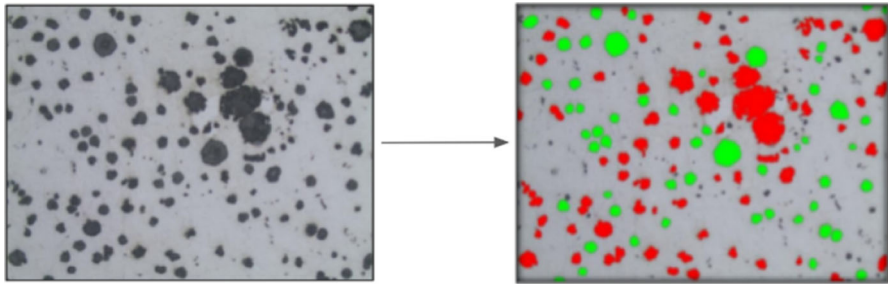
Fig. 8 Micrograph results. **a** Tension × displacement “A1”. **b** Tension × displacement “B1”. **c** Strength × displacement “A1”. **d** Strength × displacement “B1”. **e** Strength × displacement “A2”. **f** Strength × displacement “B2”. **g** Strength × displacement “A3”. **h** Strength × displacement “B3”

Table 1 Maximum approximate strength applied in the three traction tests

Sample	Test 1 (kN)	Test 2 (kN)	Test 3 (kN)	Average (kN)
A	58.692	59.368	58.692	58.917
B	62.660	62.658	62.660	62.659

Table 2 Values of Vickers microhardness tests

Test	Sample A (HV)	Sample B (HV)
1	183.86	168.41
2	176.63	174.28
3	144.63	184.46
4	180.98	180.17
5	171.44	204.02
Average	171.51	182.27

**Fig. 9** Example of sample image segmentation**Table 3** Result of image segmentation software counts

Amount of	Sample A	Sample B
Degenerated nodules	1206.50	1646.50
Normal nodules	2631	4636
Average nodules per image	93.60	153.23
Mean of degenerated nodules per image	29.43	40.16
Mean of normal nodules per image	64.17	113.17
Mean of red pixels per image	95,232	79,872
Percentage of degenerated per image	31.44%	26.21%

nodules, and the algorithm marks the degenerated nodules in red and the normal ones, in green, to facilitate counting. Figure 9 shows the results of this step.

The following measurements were made to compute the quantity of degenerated nodules: the average nodules per image, the average degenerated nodules per image, the average normal nodules per image, and the percentage of degenerated nodules in a total of 40 images. Table 3 shows the results of the CV algorithm.

The percentage of degenerated nodules presented in Table 3 is the most expressive value, but also, another variable must be considered, which is the nodule size, as shown in Fig. 9, where the “A” nodules are bigger than those of “B” and can be represented by amount of red pixels given in Table 3.

The nodules were quantified according to the Brazilian Association of Technical Standards (ABNT) MB01512. Nodules far from the edges of the image are counted as whole nodules and with at least one pixel touching the edge of the image are counted as half nodules and therefore are weighted by a factor 0.5 for the total sum of nodules.

5 Conclusions

This work proposes a computer vision (CV) algorithm to estimate the amount of degenerated graphite nodules as well as the image analysis necessary to determine the relationship between this quantity and the loss of the mechanical properties of nodular cast iron.

The difference between the hardness averages of samples “A” and “B” is only 6%. Since the values are very close, it is known that the amount of degenerated nodules does not change the hardness of the material abruptly.

Furthermore, the results showed that the number of degenerated nodules is inversely proportional to the limit of traction resistance, since the sample “A” has a greater number of degenerated nodules than sample “B” and a lower limit of traction resistance, i.e., it breaks with less force.

In a future work, a larger number of test samples as well as more images will be investigated to help solidify the conclusions of this work. An online system for characterizing metal microstructures will also be developed [9,32,34,43,47].

Acknowledgements VHCA acknowledges the sponsorship from the Brazilian National Council for Research and Development (CNPq) via Grant No. 304315/2017-6. ARA thanks the National Council for Scientific and Technological Development (CNPq, Grant #447477/2014-5, #488420/2013-0 and #304790/2015-0), in Brazil. The authors also thank Francisco Alan Xavier Mota.

References

1. Adams R, Bischof L (1994) Seeded region growing. *IEEE Trans Pattern Anal Mach Intell* 16(6):641–647
2. Afshari E, Ghambari M (2018) Predicting breakage behavior and particle size of bronze and cast iron machining chips pulverized by jet milling. *Adv Powder Technol* 29(9):2153–2160. <https://doi.org/10.1016/j.appt.2018.05.023>. <http://www.sciencedirect.com/science/article/pii/S0921883118302474>
3. Alabeedi KF, Abboud JH, Benyounis KY (2009) Microstructure and erosion resistance enhancement of nodular cast iron by laser melting. *Wear* 266(9):925–933
4. Al-Bukhaiti MA, Mohamad AAK, Emara KM, Ahmed SM (2018) Effect of slurry concentration on erosion wear behavior of AISI 5117 steel and high-chromium white cast iron. *Ind Lubr Tribol* 70(4):628–638. <https://doi.org/10.1108/ILT-07-2016-0151>
5. Benyounis K, Fakron OMA, Abboud JH, Olabi AG, Hashmi MJS (2005) Surface melting of nodular cast iron by Nd-YAG laser and TIG. *J Mater Process Technol* 170(1):127–132
6. Callister WD, Rethwisch DG (2011) *Materials science and engineering*, vol 5. Wiley, New York
7. Clement P, Angeli JP, Pineau A (1984) Short crack behaviour in nodular cast iron. *Fatigue Fract Eng Mater Struct* 7(4):251–265

8. da Candido GVM, de Melo TAA, De Albuquerque VHC, Gomes RM, de Lima SJG, Tavares JMRS (2012) Characterization of a CuAlBe alloy with different Cr contents. *J Mater Eng Perform* 21(11):2398–2406. <https://doi.org/10.1007/s11665-012-0159-6>
9. da Cruz MAA, Rodrigues JJPC, Al-Muhtadi J, Korotaev VV, de Albuquerque VHC (2018) A reference model for internet of things middleware. *IEEE Internet Things J* 5(2):871–883. <https://doi.org/10.1109/JIOT.2018.2796561>
10. Da Nobrega JA, Diniz DDS, Silva AA, Maciel TM, de Albuquerque VHC, Tavares JMRS (2016) Numerical evaluation of temperature field and residual stresses in an API 5L X80 steel welded joint using the finite element method. *Metals* 6(2):28. <https://doi.org/10.3390/met6020028>. <http://www.mdpi.com/2075-4701/6/2/28>
11. de Albuquerque VHC, de Alexandria AR, Cortez PC, Tavares JMR (2009) Evaluation of multilayer perceptron and self-organizing map neural network topologies applied on microstructure segmentation from metallographic images. *NDT & E Int* 42(7):644–651. <https://doi.org/10.1016/j.ndteint.2009.05.002>. <http://www.sciencedirect.com/science/article/pii/S0963869509000899>
12. de Albuquerque VHC, de Macedo Silva E, Leite JP, de Moura EP, de Arajo Freitas VL, Tavares JMR (2010) Spinodal decomposition mechanism study on the duplex stainless steel UNS s31803 using ultrasonic speed measurements. *Mater Des* 31(4):2147–2150. <https://doi.org/10.1016/j.matdes.2009.11.010>. <http://www.sciencedirect.com/science/article/pii/S0261306909006293>. **(Design of nanomaterials and nanostructures)**
13. de Albuquerque VHC, de Melo TAA, de Oliveira DF, Gomes RM, Tavares JMR (2010) Evaluation of grain refiners influence on the mechanical properties in a CuAlBe shape memory alloy by ultrasonic and mechanical tensile testing. *Mater Des* 31(7):3275–3281. <https://doi.org/10.1016/j.matdes.2010.02.010>. <http://www.sciencedirect.com/science/article/pii/S026130691000083X>
14. de Albuquerque VHC, Silva CC, Normando PG, Moura EP, Tavares JMR (2012) Thermal aging effects on the microstructure of Nb-bearing nickel based superalloy weld overlays using ultrasound techniques. *Mater Des* (1980–2015) 36:337–347. <https://doi.org/10.1016/j.matdes.2011.11.035>. <http://www.sciencedirect.com/science/article/pii/S0261306911007953>. **(Sustainable materials, design and applications)**
15. de Albuquerque VHC, Cortez PC, Alexandria AR, Aguiar WM, Silva EM (2007) Sistema de segmentação de imagens para quantificação de microestruturas em metais utilizando redes neurais artificiais. *Revista Matéria* 12(2):394–407
16. de Albuquerque VHC, Cortez PC, de Alexandria AR, Tavares JMR (2008) A new solution for automatic microstructures analysis from images based on a backpropagation artificial neural network. *Nondestruct Test Eval* 23(4):273–283. <https://doi.org/10.1080/10589750802258986>
17. de Albuquerque VHC, Filho PR, Cavalcante TS, Tavares JMR (2010) New computational solution to quantify synthetic material porosity from optical microscopic images. *J Microsc* 240(1):50–59
18. de Albuquerque VHC, Tavares JMRS, Duro LM (2010) Evaluation of delamination damage on composite plates using an artificial neural network for the radiographic image analysis. *J Compos Mater* 44(9):1139–1159. <https://doi.org/10.1177/0021998309351244>
19. de Albuquerque VHC, Silva CC, Menezes TIdS, Farias JP, Tavares JMR (2011) Automatic evaluation of nickel alloy secondary phases from SEM images. *Microsc Res Tech* 74(1):36–46
20. de Albuquerque V, Barbosa C, Silva C, Moura E, Filho P, Papa J, Tavares J (2015) Ultrasonic sensor signals and optimum path forest classifier for the microstructural characterization of thermally-aged inconel 625 alloy. *Sensors* 15(6):12474. <https://doi.org/10.3390/s150612474>
21. de Araújo Freitas VL, de Albuquerque VHC, de Macedo Silva E, Silva AA, Tavares JMR (2010) Nondestructive characterization of microstructures and determination of elastic properties in plain carbon steel using ultrasonic measurements. *Mater Sci Eng A* 527(16):4431–4437. <https://doi.org/10.1016/j.msea.2010.03.090>. <http://www.sciencedirect.com/science/article/pii/S0921509310003771>
22. de Araújo Freitas VL, Normando PG, de Albuquerque VHC, de Macedo Silva E, Silva AA, Tavares JMRS (2011) Nondestructive characterization and evaluation of embrittlement kinetics and elastic constants of duplex stainless steel SAF 2205 for different aging times at 425°C and 475°C. *J Nondestruct Eval* 30(3):130–136. <https://doi.org/10.1007/s10921-011-0100-1>
23. de Macedo Silva E, Leite JP, de França Neto FA, Leite JP, Fialho WM, de Albuquerque VHC, Tavares JMR (2014) Evaluation of the magnetic permeability for the microstructural characterization of a duplex stainless steel. *J Test Eval* 44(3):1106–1111

24. de Macedo Silva E, Leite JP, Leite JP, Fialho WML, de Albuquerque VHC, Tavares JMRS (2016) Induced magnetic field used to detect the sigma phase of a 2205 duplex stainless steel. *J Nondestruct Eval* 35(2):28. <https://doi.org/10.1007/s10921-016-0339-7>
25. de Macedo Silva E, de Albuquerque VHC, Leite JP, Varela ACG, de Moura EP, Tavares JMR (2009) Phase transformations evaluation on a UNS s31803 duplex stainless steel based on nondestructive testing. *Mater Sci Eng A* 516(1):126–130. <https://doi.org/10.1016/j.msea.2009.03.004>. <http://www.sciencedirect.com/science/article/pii/S0921509309003293>
26. de Silva PMO, de Abreu HFG, de Albuquerque VHC, de Lima Neto P, Tavares JMR (2011) Cold deformation effect on the microstructures and mechanical properties of AISI 301LN and 316L stainless steels. *Mater Des* 32(2):605–614. <https://doi.org/10.1016/j.matdes.2010.08.012>. <http://www.sciencedirect.com/science/article/pii/S0261306910004875>
27. de Albuquerque VHC, de Melo TAA, Gomes RM, de Lima SJG, Tavares JMR (2010) Grain size and temperature influence on the toughness of a CuAlBe shape memory alloy. *Mater Sci Eng A* 528(1):459–466. <https://doi.org/10.1016/j.msea.2010.09.034>. <http://www.sciencedirect.com/science/article/pii/S0921509310010646>. **(Special topic section: local and near surface structure from diffraction)**
28. DeCost BL, Francis T, Holm EA (2018) High throughput quantitative metallography for complex microstructures using deep learning: a case study in ultrahigh carbon steel. *arXiv preprint arXiv:1805.08693*
29. Duro LMP, Tavares JMR, de Albuquerque VHC, Goncalves DJ (2013) Damage evaluation of drilled carbon/epoxy laminates based on area assessment methods. *Compos Struct* 96:576–583. <https://doi.org/10.1016/j.compstruct.2012.08.003>. <http://www.sciencedirect.com/science/article/pii/S0263822312003674>
30. Gupta G (2011) Algorithm for image processing using improved median filter and comparison of mean, median and improved median filter. *Int J Soft Comput Eng (IJSCE)* 1(5):304–311
31. Jailin C, Bouterf A, Poncelet M, Roux S (2017) In situ μ ct-scan mechanical tests: fast 4d mechanical identification. *Exp Mech* 57(8):1327–1340
32. Lakshmanaprabu SK, Shankar K, Khanna A, Gupta D, Rodrigues JJPC, Pinheiro PR, Albuquerque VHCD (2018) Effective features to classify big data using social internet of things. *IEEE Access* 6:24196–24204. <https://doi.org/10.1109/ACCESS.2018.2830651>
33. Lal R, Singh RC (2018) Experimental comparative study of chrome steel pin with and without chrome plated cast iron disc in situ fully flooded interface lubrication. *Surf Topogr Metrol Prop* 6(3):035,001. <http://stacks.iop.org/2051-672X/6/i=3/a=035001>. Accessed 20 May 2018
34. Mahmoud MME, Rodrigues JJPC, Ahmed SH, Shah SC, Al-Muhtadi JF, Korotaev VV, Albuquerque VHCD (2018) Enabling technologies on cloud of things for smart healthcare. *IEEE Access* 6:31950–31967. <https://doi.org/10.1109/ACCESS.2018.2845399>
35. Nadot Y, Mendez J, Ranganathan N, Beranger AS (1999) Fatigue life assessment of nodular cast iron containing casting defects. *Fatigue Fract Eng Mater Struct (UK)* 22(4):289–300
36. Nunes TM, de Albuquerque VHC, Papa JP, Silva CC, Normando PG, Moura EP, Tavares JMR (2013) Automatic microstructural characterization and classification using artificial intelligence techniques on ultrasound signals. *Expert Syst Appl* 40(8):3096–3105. <https://doi.org/10.1016/j.eswa.2012.12.025>. <http://www.sciencedirect.com/science/article/pii/S0957417412012663>
37. Ochi Y, Masaki K, Matsumura T, Sekino T (2001) Effect of shot-peening treatment on high cycle fatigue property of ductile cast iron. *Int J Fatigue* 23(5):441–448
38. Otsu N (1979) A threshold selection method from gray-level histograms. *IEEE Trans Syst Man Cybern* 9(1):62–66
39. Papa JP, Nakamura RY, de Albuquerque VHC, Falco AX, Tavares JMR (2013) Computer techniques towards the automatic characterization of graphite particles in metallographic images of industrial materials. *Expert Syst Appl* 40(2):590–597. <https://doi.org/10.1016/j.eswa.2012.07.062>. <http://www.sciencedirect.com/science/article/pii/S0957417412009189>
40. Papa JP, Nakamura RYM, de Albuquerque VHC, Falcão AX, Tavares JMRS (2013) Computer techniques towards the automatic characterization of graphite particles in metallographic images of industrial materials. *Expert Syst Appl* 40(2):590–597. <https://doi.org/10.1016/j.eswa.2012.07.062>
41. Peixoto FdM, Rebouças EdS, Xavier FGdL, Rebouças Filho PP (2015) Software development for ductile cast iron graphite nodules density calculation using digital image processing. *Matéria (Rio de Janeiro)* 20(1):262–272

42. Rebouas Filho PP, da Silveira Cavalcante T, de Albuquerque VHC, Tavares JMR (2009) Brinell and vickers hardness measurement using image processing and analysis techniques. *J Test Eval* 38(1):88–94
43. Rodrigues JJPC, Segundo DBDR, Junqueira HA, Sabino MH, Prince RM, Al-Muhtadi J, Albuquerque VHCD (2018) Enabling technologies for the internet of health things. *IEEE Access* 6:13129–13141. <https://doi.org/10.1109/ACCESS.2017.2789329>
44. Silva E, Marinho L, Filho P, Leite J, Leite J, Fialho W, de Albuquerque V, Tavares J (2016) Classification of induced magnetic field signals for the microstructural characterization of sigma phase in duplex stainless steels. *Metals* 6(7):164. <https://doi.org/10.3390/met6070164>
45. Silva E, Paula A, Leite J, Leite J, Andrade L, de Albuquerque V, Tavares J (2016) Detection of the magnetic easy direction in steels using induced magnetic fields. *Metals* 6(12):317. <https://doi.org/10.3390/met6120317>
46. Silva CC, de Albuquerque VHC, Miná EM, Moura EP, Tavares JMRS (2018) Mechanical properties and microstructural characterization of aged nickel-based alloy 625 weld metal. *Metall Mater Trans A* 49(5):1653–1673. <https://doi.org/10.1007/s11661-018-4526-2>
47. Silva A, Juc S, Costa L, Silva P, Pereira R (2018) Versatile IoT system for cloud-based sensor monitoring. *J Mechatron Eng* 1(1):2–10. <https://doi.org/10.1234/jme.v1i1.8>. <http://jme.ojs.galoa.net.br/index.php/jme/article/view/8>
48. Taheri S, Vedenbaum A, Nicolau A, Hu N, Haghighat MR (2018) Opencv.js: Computer Vision processing for the open web platform. In: *Proceedings of the 9th ACM Multimedia Systems Conference, MMSys '18*. ACM, New York, pp 478–483. <https://doi.org/10.1145/3204949.3208126>